materials

MDPI

Article

Computational Study of Novel Semiconducting Sc_2CT_2 (T = F, Cl, Br) MXenes for Visible-Light Photocatalytic Water Splitting

Shaoying Guo [1,2,*], Hao Lin [1], Jiapeng Hu [1], Zhongliang Su [3] and Yinggan Zhang [4,*]

[1] Fujian Provincial Key Laboratory of Eco-Industrial Green Technology, College of Ecology and Resource Engineering, Wuyi University, Wuyishan 354300, China; linhaosg@wuyiu.edu.cn (H.L.); wqhjp@wuyiu.edu.cn (J.H.)
[2] Fujian Provincial Key Laboratory of Pollution Control & Resource Reuse, Fujian Normal University, Fuzhou 350007, China
[3] Xiamen Products Quality Supervision & Inspection Institute, Xiamen 361005, China; suzhongliang@xmzjy.org
[4] College of Materials, Fujian Provincial Key Laboratory of Theoretical and Computational Chemistry, Xiamen University, Xiamen 361005, China
* Correspondence: wyxygshy@wuyiu.edu.cn (S.G.); ygzhang@xmu.edu.cn (Y.Z.)

Abstract: Seeking candidate photocatalysts for photocatalytic water splitting, via visible light, is of great interest and importance. In this study, we have comprehensively explored the crystal structures, electronic properties, and optical absorbance of two-dimensional (2D) Sc_2CT_2 (T = F, Cl, Br) MXenes and their corresponding photocatalytic water splitting, under the visible-light region, by first-principles calculations. Herein, we have proposed that 2D Sc_2CT_2 MXenes can be fabricated from their layered bulk compounds, alternatively to the traditional chemical etching method. Creatively, we proposed Sc_2CT_2 (T = F, Br) as new materials; the band edge alignments of Sc_2CF_2 can be tuned to meet the water redox potentials at pH = 8.0. It is highlighted that Sc_2CF_2 shows outstanding optical spectra harvested under visible-light wavelength regions, and efficient separation of photo-induced electrons and holes in different zones. These present results provide eloquent evidence and open a new door on the photocatalysis applications of such novel semiconducting MXenes.

Keywords: MXenes; photocatalyst; first-principles calculations

check for updates

Citation: Guo, S.; Lin, H.; Hu, J.; Su, Z.; Zhang, Y. Computational Study of Novel Semiconducting Sc_2CT_2 (T = F, Cl, Br) MXenes for Visible-Light Photocatalytic Water Splitting. *Materials* **2021**, *14*, 4739. https://doi.org/10.3390/ma14164739

Academic Editor: Juan M. Coronado

Received: 11 July 2021
Accepted: 20 August 2021
Published: 22 August 2021

Publisher's Note: MDPI stays neutral with regard to jurisdictional claims in published maps and institutional affiliations.

Copyright: © 2021 by the authors. Licensee MDPI, Basel, Switzerland. This article is an open access article distributed under the terms and conditions of the Creative Commons Attribution (CC BY) license (https://creativecommons.org/licenses/by/4.0/).

1. Introduction

Hydrogen production, through photocatalytic water splitting via visible-light irradiation, is a promising solution to solve the environmental issues by achieving low-cost, nonpolluting, and environmentally friendly energy [1,2]. A suitable photocatalyst must fulfill at least the following three requirements: moderate band gaps, appropriate band alignments, and efficient separation of photo-generated electron–hole pairs. This is to say, the band gap of the semiconductor photocatalyst must straddle the redox potential of water, as follows: the conduction band minimum (CBM) must be higher than −4.44 eV, which is the redox potential of H^+/H_2; and the valence band maximum (VBM) must be lower than −5.67 eV, which is the redox potential of H_2O/O_2 [3–5]. Accordingly, 1.23 eV is the smallest band gap for a semiconductor photocatalyst. To exploit solar radiation more efficiently, a value of around 1.8 eV is an ideal gap for an efficient photocatalyst [2,6,7]. Moreover, the efficiency of a photocatalyst must always be hampered by the recombination of photo-induced electron–hole pairs. Therefore, the efficient carrier separation is another vital point in semiconductor photocatalysts. However, finding an efficient semiconductor photocatalyst for hydrogen generation, to meet all the above requirements, is still an ongoing challenge [5].

Recently, two-dimensional (2D) transition metal carbides/nitrides (MXene) were produced from their corresponding MAX phases, where M stands for early transition metal, A stands for IIIA or IVA element, and X represents C or N [8–16]. MXenes have been extensively explored for miscellaneous applications as photocatalysts [17–19], electromagnetic

interference shielding [20], battery anodes [21,22], heavy-metal removal [23], etc. Especially, for the photocatalytic community, monolayer Zr_2CO_2 and Hf_2CO_2 MXenes have been evaluated as semiconductor photocatalysts. They not only exhibit suitable band gaps and band alignments, but can also separate photo-generated electrons and holes effectively [17–19]. Except for Zr_2CO_2 and Hf_2CO_2, the semiconducting feature was characterized in some other Sc-based MXenes, such as Sc_2CO_2 and $Sc_2C(OH)_2$, which possess the band gaps of 2.96 eV and 0.77 eV, respectively [24,25]. Experimentally, a layered Sc_2CCl_2 bulk crystal, with a unit cell that is isostructural to a 2D MXene, was successfully synthesized, which implied the feasibility for the fabrication of monolayer Sc_2CCl_2 [26]. Theoretically, the calculated optical bandgap of one-layer (1 L), 2 L and 3 L Sc_2CCl_2 is about 1.5 eV by the GW + RPA method [27]. Accordingly, the monolayer Sc_2CCl_2 is a promising optoelectronic material, due to the excellent light absorbance [27]. In addition, the analogue bulk crystal Y_2CF_2 has been directly synthesized through a high-temperature solid-state reaction a while ago [28,29]. The crystal has the ability to photo-reduce protons into H_2 in the range of visible light [28]. Inspired by these studies, and considering the analogous of F, Cl, and Br, we wonder if Sc_2CT_2 MXenes (T = F, Cl, Br) are endowed with outstanding features as efficient semiconductor photocatalysts for water splitting.

Thanks to the progress of the density functional theory, the computational method is now a very important approach for designing new functional material. In the present work, we have comprehensively explored the exfoliate energy, geometrical structure, kinetic and thermal stabilities, as well as electronic properties and optical absorbance of 2D Sc_2CT_2 (T = F, Cl, Br) MXenes, using first-principles calculations. Especially, we have extensively explored the possibility of Sc_2CT_2 (T = F, Cl, Br) MXenes to be used for visible-light photocatalytic water splitting. Our study can make contributions to the discovery and applications of Sc-based MXenes, as semiconductor photocatalysts for water-splitting hydrogen production.

2. Methods

Our first-principles calculations were performed using the projector augmented-wave (PAW) [30] of generalized gradient approximation (GGA) with Perdew–Burke–Ernzerhof (PBE) [31] formalism, implemented in the Vienna ab initio simulation package (VASP) [32,33]. The energy cutoff of the plane-wave expansion was 550 eV. The thickness of the vacuum space was 25 Å in the z direction. The reciprocal space was represented by a Monkhorst-Pack scheme with $11 \times 11 \times 1$ k-point grid meshes. The convergence criteria of energy for both electrons and ions were, respectively, 1×10^{-5} eV and 1×10^{-6} eV. Phonon dispersions were retrieved by the density functional perturbation theory (DFPT) as embedded in the PHONOPY code to study the kinetic stability [34,35], for which a $4 \times 4 \times 1$ supercell with $4 \times 4 \times 1$ k-point grid meshes was employed. The DFT-D3 van der Waals (vdW)-corrected methods [36] were performed for the improved descriptions of the layered bulk crystals. The calculation results were dealt by the ALKEMIE code [37]. To obtain accurate dielectric functions, we employed the time-dependent Hartree–Fock calculations (TDHF) [38] by the Heyd–Scuseria–Ernzerhof (HSE06) [39] calculations, which have taken the excitonic effects into account.

3. Results and Discussion

First, the bulk and monolayer structures of Sc_2CT_2 (T = F, Cl, Br) are displayed in Figure 1. The bulk phase is crystallized in the trigonal space group of $P\bar{3}m1$, in which the upper and lower sides of the Sc_2C plane are halogenated by two T atomic layers. Moreover, the center C atoms are coordinated by six Sc atoms, leading to an octahedron of Sc_6C. Table 1 lists the calculated lattice parameters a (Å) and Sc–C bond lengths L (Å) of the Sc_6C octahedron of the monolayer Sc_2CT_2. The lattice parameters a (Å) and c (Å) of the bulk Sc_2CT_2 are listed for comparison as well. According to our calculations, the lattice constant, via the structural optimization for bulk Sc_2CCl_2, is 3.445 Å, which is in line with the experimental result [26]. As the surface groups change from F to Br, the

lattice parameters increase slightly, which is attributed to the raising of the halogen element atomic radius. In the Sc_6C octahedron of the monolayer Sc_2CT_2, the changes in the Sc–C bond lengths show the same trend as the surface groups from F to Br. It is worth noting that the calculated lattice parameters *a* of the monolayer Sc_2CT_2 are almost identical with that of their bulk phases, indicating that the interlayer interaction between the atomic layers are very weak. Thus, the monolayer Sc_2CT_2 is likely to be isolated from the corresponding bulk phase.

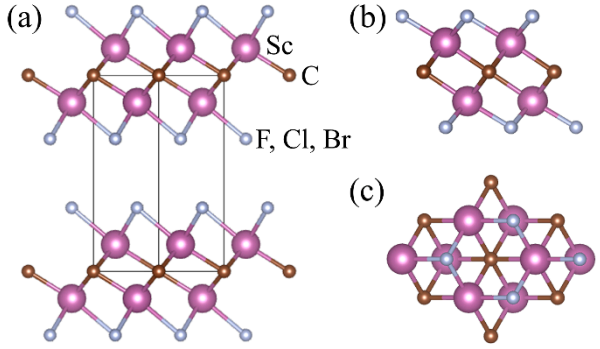

Figure 1. (**a**) Crystal structure of bulk Sc_2CT_2 (T = F, Cl, Br). (**b**) Side view and (**c**) top view of single-layer Sc_2CT_2.

Table 1. The calculated lattice parameters *a* (Å) and *c* (Å) of bulk Sc_2CT_2, the lattice parameters *a* (Å) and Sc–C bond lengths *L* (Å) of monolayer Sc_2CT_2.

		Sc_2CF_2	Sc_2CCl_2	Sc_2CBr_2
Bulk	*a*	3.285	3.445	3.498
	c	6.481	8.854	9.295
Monolayer	*a*	3.252	3.431	3.507
	L	2.266	2.330	2.358

Herein, the 3D bulk crystals are composed of stacked MXene sheets, as displayed in Figure 1. Distinct from the traditional chemical etching method to fabricate MXene, which is environmentally unfriendly, owing to the using of hydrofluoric acid (HF), we introduce an alternative isolation approach, which has been successfully used for graphene manufacturing. Figure 2 displays the calculated exfoliation energy of Sc_2CT_2, and the exfoliation energy of graphite is also shown as a benchmark. As is observed, the evaluated exfoliation energy of graphite is ~0.32 J/m^2, according to our calculation, which is consistent with the experimental measurement and previous theoretical study [40,41]. Amazedly, the calculated exfoliation energies for all the explored Sc_2CT_2 are much lower than that of graphite, suggesting that the monolayer Sc_2CT_2 is very likely to be obtained from its bulk phases, by similar experimental methods as graphene. Especially, the exfoliation energy of Sc_2CF_2 is only ~0.23 J/m^2. Such value is nearly two-thirds of that for graphite, indicating the ranking possibility for experimental fabrication.

The stability acts a pivotal part in the practical application and experimental fabrication of 2D Sc_2CT_2. Therefore, the phonon dispersion spectra calculations were employed, to assess the kinetic stabilities of 2D Sc_2CT_2. Moreover, ab initio molecular dynamics (AIMD) calculations were adopted, to evaluate the thermal stabilities. As the phonon curves illustrated in the upper panel of Figure 3, there is not any appreciable imaginary acoustic dispersion branch of the phonon curve for all the Sc_2CT_2, confirming the kinetic stabilities of the three monolayer MXenes. More importantly, the highest phonon spectra frequencies of all the investigated Sc_2CT_2 are up to 20 THz. This value is comparable with that of the other monolayer material, implying the rough junction among the Sc, C, and T atoms [19]. The total energy changes and structure snapshots at 300 K, sustaining 9 ps

of Sc_2CT_2, are displayed in the lower panel of Figure 3. As is shown, the total energies are swinging very slightly and the atoms are well maintained around their equilibrium positions under the temperature field, indicating the thermal stabilities of the monolayer Sc_2CT_2. Hence, the kinetic stabilities and thermal stabilities of the Sc_2CT_2 monolayer have been approved.

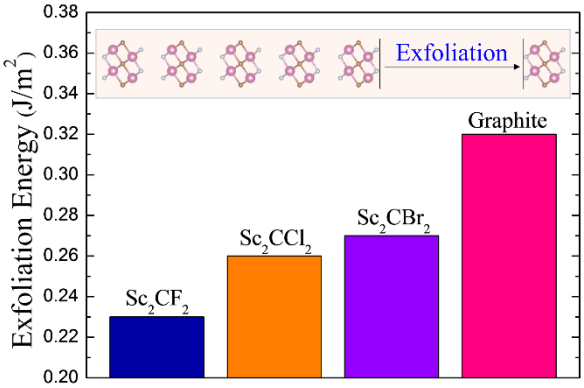

Figure 2. The calculated exfoliation energies of 2D Sc_2CT_2 and graphite. The inset is the schematic of exfoliation process.

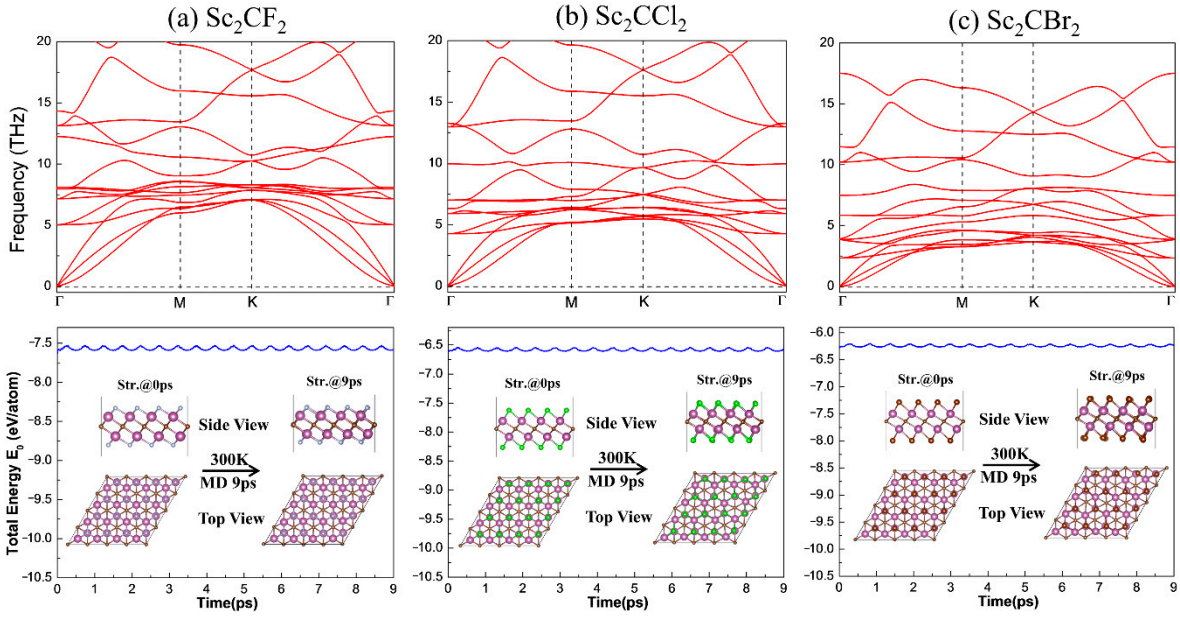

Figure 3. Phonon dispersion curves (upper panel), total energy changes and structure snapshots (lower panel) from 0 to 9 ps from AIMD calculations for (**a**) Sc_2CF_2, (**b**) Sc_2CCl_2, and (**c**) Sc_2CBr_2.

To understand the electronic properties of monolayer Sc_2CT_2, the total and partial density of states (DOS) are represented in Figure 4. Note that the DOS of Sc_2CF_2, Sc_2CCl_2, and Sc_2CBr_2 exhibit very similar features, which is in relation to their alike atomic configurations. For the explored Sc_2CF_2 and Sc_2CCl_2, the CBM is mainly contributed by Sc 3*d* states, while the VBM is entirely dominated by C 2*p* states and Sc 3*d* states. In addition, the C 2*p* orbits and Sc 3*d* orbits are forcefully hybridized [42]. The CBM of Sc_2CBr_2 is contributed by Sc 3*d* states as well, but the VBM of it is not only dominated by C 2*p* states and Sc 3*d* states, but also contributed by Br 4*p* states. Moreover, the calculated band gaps for Sc_2CF_2, Sc_2CCl_2, and Sc_2CBr_2 are 1.85 eV, 1.70 eV, and 1.54 eV, respectively, which are endowed with high harvest under the visible-light region. Note that the band gaps of all three 2D Sc_2CT_2 are larger than 1.23 eV, which meet the minimum value required

for an efficient photocatalyst. Hence, it can be concluded that all the Sc_2CT_2 MXenes are promising candidates as semiconductor photocatalysts, in the aspect of bandgaps.

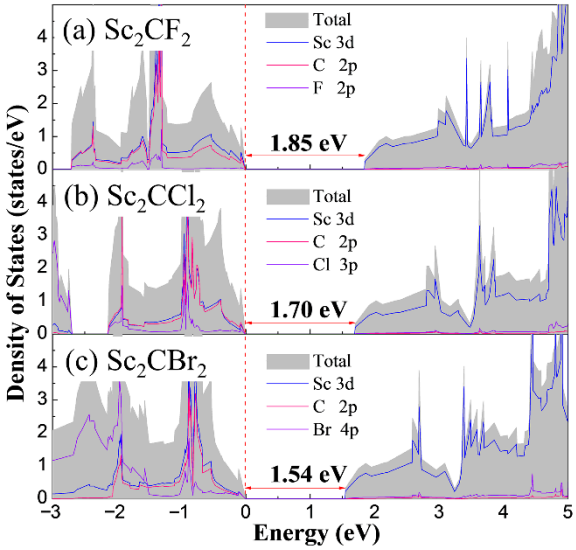

Figure 4. The total and partial density of states of (**a**) Sc_2CF_2, (**b**) Sc_2CCl_2, and (**c**) Sc_2CBr_2. The Fermi energy is marked by dashed lines.

Besides the bandgap size, band edge alignments are another predominant factor to facilitate the water reaction. We have therefore calculated the band edge alignments of Sc_2CT_2 in Figure 5, to assess the performance of these newly designed photocatalysts. According to the band alignments in Figure 5, 2D Sc_2CCl_2 and Sc_2CBr_2 exhibit very similar band edge alignment characters. Interestingly, the VBM of Sc_2CCl_2 and Sc_2CBr_2 are located at a more positive potential than the water redox potential of H_2O/O_2 (1.23 eV vs. normal hydrogen electrode, NHE), implying the remarkable oxidation capabilities of the photo-generated holes. This advantage can be applied in capturing the electrons from organic pollutants, such as methylene blue [19]. However, it is a pity that the CBMs of Sc_2CT_2 are also located at a more positive potential than the redox potential of H^+/H_2 (0 V vs. NHE), indicating that they are not appropriate for photocatalytic water splitting. While for Sc_2CF_2, the CBM is much more negative than the redox potential of H^+/H_2 (0 V vs. NHE), but the VBM position is not more positive than the redox potential of O_2/H_2O (1.23 eV vs. NHE), suggesting the unapplicable band alignments for water splitting. From the above analysis, one can observe that the band positions of 2D Sc_2CF_2, Sc_2CCl_2 and Sc_2CBr_2 are not suitable as semiconductor photocatalysts under ambition conditions.

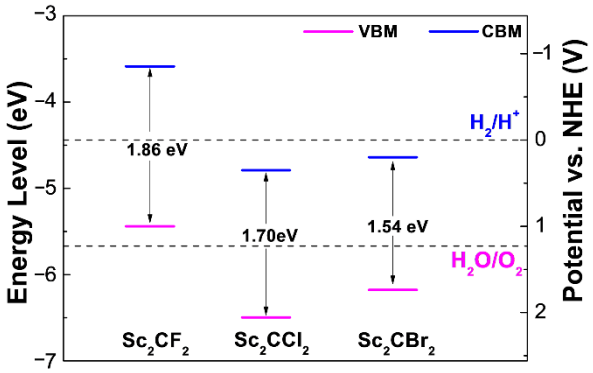

Figure 5. Band alignments with respect to the water reduction and oxidation potential levels of Sc_2CT_2 MXenes.

From Figure 5, the band alignments of Sc_2CF_2 are not appropriate under ambient conditions. However, in the practical application of a photocatalysis, the water redox potential is related to the value of pH in the solutions. Hence, the water oxidation potential of O_2/H_2O can be expressed by the following equation [43]:

$$E^{OX}_{O_2/H_2O} = -5.67\ \text{eV} + \text{pH} \times 0.059\ \text{eV} \quad (1)$$

According to Equation (1), one can shift the oxidation level of water upward in Figure 5. Thus, the band edge alignments of Sc_2CF_2 can be tuned to straddle the redox potential of water. As illustrated in Figure 6, in ambient conditions, Sc_2CF_2 is not an appropriate photocatalyst, due to its unsuitable band edge alignments. While in a pH = 8.0 solution, the oxidation level and the reduction potential of water will shift upwards by 0.472 V. We have plotted the band alignments of Sc_2CF_2 in Figure 6, from which one can observe that the VBM locates more positively than the hydrogen reduction level (0 V vs. NHE), and the CBM locates more negatively than the oxygen oxidation level (1.23 eV vs. NHE). The results show that Sc_2CF_2 has a favorable band position for water splitting in a pH = 8.0 solution. Moreover, the energy difference between VBM and the oxygen reduction potential (oxidizing power) of Sc_2CF_2 is 0.25 eV, and the energy difference between CBM and the hydrogen reduction potential (reducing power) is 0.38 eV. Furthermore, we can moderate the water-oxidizing power and reducing power of Sc_2CF_2 by changing the pH to 9.0. Notably, the oxidizing power increases to 0.31 eV, while the reducing power decreases to 0.32 eV. Such values suggest that Sc_2CF_2 has excellent band edge positions as photocatalysts, which is very helpful for protecting the chemical equilibriums during the water-splitting reaction process.

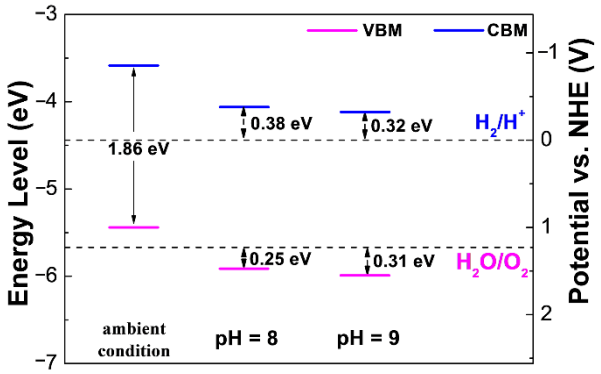

Figure 6. Band alignments with respect to water redox potentials of Sc_2CF_2 in ambient conditions, pH = 8 solution, and pH = 9 solution.

Having confirmed the band gap and band edge alignments of Sc_2CF_2, we now turn to its optical spectra in the visible-light wavelength range, which is another vital criteria for photocatalysts to drive the water-splitting reaction efficiently. Figure 7 displays the optical absorbance of Sc_2CF_2, obtained from TDHF-HSE06 and DFT-HSE06, and the light spectrum of silicon is plotted as a benchmark [44]. As is observed, the calculated optical absorbance of 2D Sc_2CF_2 are absolutely higher than that of silicon, in most visible-light regions. Moreover, the optical absorption, obtained by the TDHF-HSE06 method, is significantly larger than that evaluated by the standard DFT-HSE06 approach, which implies a strong excitonic effect in Sc_2CF_2, in the visible-light region. For the absorption coefficients that were evaluated by the TDHF-HSE06 method, 2D Sc_2CF_2 exhibits broad optical absorptions, with three optical spectra peaks at around ~400 nm, ~450 nm, and ~550 nm. It is worth noting that the optical coefficients of Sc_2CF_2 can reach up to ~2×10^5 cm^{-1} at around ~550 nm, suggesting an extraordinary light harvesting ability. The outstanding optical performances imply that the Sc_2CF_2 monolayer is a very hopeful candidate as a semiconductor photocatalyst for hydrogen generation.

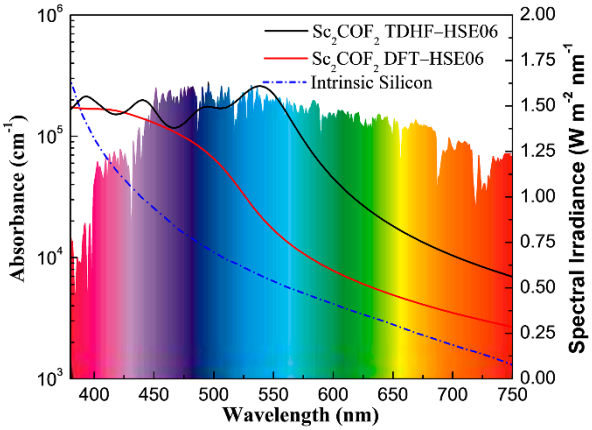

Figure 7. Calculated optical absorption coefficients of Sc_2CF_2 compared with the experimental spectrum of intrinsic silicon. The colorful background is the reference solar spectral irradiance [45].

The efficient separation of photo-induced electrons and holes can guarantee high efficiency of a semiconductor photocatalyst. Figure 8a shows the electron localization functions (ELFs) of 2D Sc_2CF_2, to investigate the spatial charge distributions. As presented in Figure 8a, the electrons are transferred from Sc atoms to C atoms and F atoms, and completely gathered around C atoms and F atoms, leading to highly localized surroundings. Accordingly, the positively charged region around the Sc atoms will attract the photo-generated electrons, while the negatively charged region around the C and F atoms will trap the photo-activated holes. Hence, the photo-induced electron–hole pairs tend to aggregated in different areas, resulting in efficient carrier separation in the Sc_2CF_2 monolayer. As is known, most photo-generated electrons are gathered at the CBM, and photo-generated holes are gathered at the VBM [4,46]. We have then computed the band decomposed charge density of the Sc_2CF_2 material in Figure 8. From the band decomposed charge density, we can observe that the CBMs are entirely contributed by the *d* electrons from the Sc atoms, while the VBMs are completely dominated by the Sc atoms and *p* electrons from the C atoms, which is in line with the partial DOS that is displayed in Figure 4a. As is observed, the CBMs are mainly distributed at the Sc–F zones, and the VBM are located at the C zones, thus the photo-induced electrons and holes will transfer to the Sc–F zones and C zones, respectively. Therefore, the photo-excited electron–hole pairs can be separated efficiently at different zones in the monolayer Sc_2CF_2, which is a benefit for the photocatalysis water-splitting reaction on the monolayer Sc_2CF_2 photocatalyst.

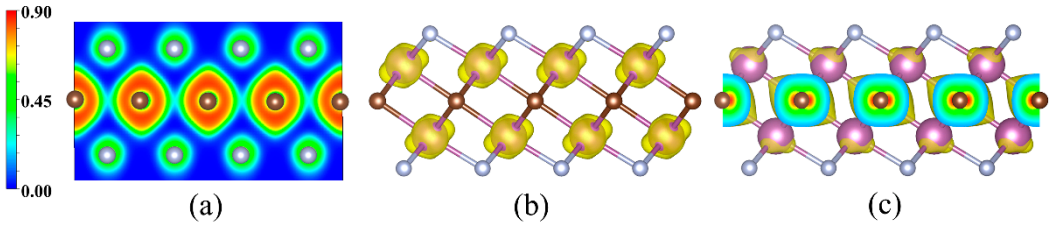

Figure 8. (**a**) The ELF contour plot perpendicular to the (100) direction for 2D Sc_2CF_2. The band decomposed charge density of the (**b**) CBM and (**c**) VBM for 2D Sc_2CF_2.

4. Conclusions

In conclusion, we have comprehensively explored the photocatalytic water splitting of Sc_2CT_2 (T = F, Cl, Br) MXenes, as semiconductor photocatalysts for hydrogen generation, based on first-principles calculations. Firstly, the exfoliation energy of bulk-layered Sc_2CT_2 has been calculated, which is much smaller than that of graphite, implying that the monolayer Sc_2CT_2 can be isolated by mechanical cleavage from its bulk phases. Additionally,

as demonstrated by phonon calculations and ab initio molecular dynamicssimulations, the Sc_2CT_2 monolayer shows kinetic and thermal stabilities. Moreover, the calculated band gaps for Sc_2CF_2, Sc_2CCl_2, and Sc_2CBr_2 are 1.85 eV, 1.70 eV, and 1.54 eV, respectively. However, in ambient conditions, Sc_2CT_2 is not a suitable photocatalyst, due to its inappropriate band edge position. It is highlighted that the band edge alignments of Sc_2CF_2 can be tuned to straddle the redox potential of water, by shifting the oxidation level of water upwards, which can be realized by introducing a pH = 8.0 solution. Furthermore, by changing the pH to 9.0, the oxidizing power and reducing power of Sc_2CF_2 can be moderated to a harmonious level, which is very helpful to keep the chemical balance during the redox reaction. Meanwhile, 2D Sc_2CF_2 exhibits a high optical absorption, up to 2×10^5 cm^{-1}, in visible-light wavelengths. Notably, the photo-excited electron–hole pairs of Sc_2CF_2 will separate efficiently. Our exciting results pave the way for designing more MXenes as semiconductor photocatalysts for hydrogen generation.

Author Contributions: Conceptualization, S.G. and Y.Z.; methodology, S.G. and Y.Z.; validation, S.G. and Y.Z.; formal analysis, S.G. and Y.Z.; investigation, H.L., J.H. and Z.S.; writing—original draft preparation, S.G.; writing—review and editing, Y.Z.; visualization, H.L., J.H. and Z.S.; supervision, Y.Z.; funding acquisition, S.G. All authors have read and agreed to the published version of the manuscript.

Funding: This work is financially supported by Natural Science Foundation of Fujian Province (2020J01411), Young and middle-aged Scientific Research Project of Education Department of Fujian Province (JAT190773), Scientific Research Fund project of Wuyi University (XD201703) and Fujian Provincial Key Laboratory of Pollution Control & Resource Reuse Open Project Fund.

Institutional Review Board Statement: Not applicable.

Informed Consent Statement: Not applicable.

Data Availability Statement: Data available on request. The data presented in this study are available on request from the corresponding author.

Conflicts of Interest: The authors declare no conflict of interest.

References

1. Simon, T.; Bouchonville, N.; Berr, M.J.; Vaneski, A.; Adrović, A.; Volbers, D.; Wyrwich, R.; Döblinger, M.; Susha, A.S.; Rogach, A.L.; et al. Redox shuttle mechanism enhances photocatalytic H_2 generation on Ni-decorated CdS nanorods. *Nat. Mater.* **2014**, *13*, 1013–1018. [CrossRef] [PubMed]
2. Chen, X.; Liu, L.; Peter, Y.Y.; Mao, S.S. Increasing solar absorption for photocatalysis with black hydrogenated titanium dioxide nanocrystals. *Science* **2011**, *331*, 746–750. [CrossRef] [PubMed]
3. Sa, B.; Li, Y.-L.; Qi, J.; Ahuja, R.; Sun, Z. Strain engineering for phosphorene: The potential application as a photocatalyst. *J. Phys. Chem. C* **2014**, *118*, 26560–26568. [CrossRef]
4. Zhang, Y.; Sa, B.; Zhou, J.; Sun, Z. Two-dimensional $(Zr_{0.5}Hf_{0.5})_2CO_2$: A promising visible light water-splitting photocatalyst with efficiently carrier separation. *Comput. Mater. Sci.* **2021**, *186*, 110013. [CrossRef]
5. Singh, A.K.; Mathew, K.; Zhuang, H.L.; Hennig, R.G. Computational screening of 2D materials for photocatalysis. *J. Phys. Chem. Lett.* **2015**, *6*, 1087–1098. [CrossRef] [PubMed]
6. Ran, J.; Zhang, J.; Yu, J.; Jaroniec, M.; Qiao, S.Z. Earth-abundant cocatalysts for semiconductor-based photocatalytic water splitting. *Chem. Soc. Rev.* **2014**, *43*, 7787–7812. [CrossRef]
7. Asahi, R.; Morikawa, T.; Irie, H.; Ohwaki, T. Nitrogen-doped titanium dioxide as visible-light-sensitive photocatalyst: Designs, developments, and prospects. *Chem. Rev.* **2014**, *114*, 9824–9852. [CrossRef]
8. Lei, J.C.; Zhang, X.; Zhou, Z. Recent advances in MXene: Preparation, properties, and applications. *Front. Phys.* **2015**, *10*, 276–286. [CrossRef]
9. Zhan, X.; Si, C.; Zhou, J.; Sun, Z. MXene and MXene-based composites: Synthesis, properties and environment-related applications. *Nanoscale Horiz.* **2020**, *5*, 235–258. [CrossRef]
10. Khazaei, M.; Ranjbar, A.; Arai, M.; Sasaki, T.; Yunoki, S. Electronic properties and applications of MXenes: A theoretical review. *J. Mater. Chem. C* **2017**, *5*, 2488–2503. [CrossRef]
11. Wang, H.; Peng, R.; Hood, Z.D.; Naguib, M.; Adhikari, S.P.; Wu, Z. Titania composites with 2D transition metal carbides as photocatalysts for hydrogen production under visible-light irradiation. *ChemSusChem* **2016**, *9*, 1490–1497. [CrossRef]
12. Anasori, B.; Lukatskaya, M.R.; Gogotsi, Y. 2D metal carbides and nitrides (MXenes) for energy storage. *Nat. Rev. Mater.* **2017**, *2*, 1–17. [CrossRef]

13. Xiong, P.; Sun, B.; Sakai, N.; Ma, R.; Sasaki, T.; Wang, S.; Zhang, J.; Wang, G. 2D superlattices for efficient energy storage and conversion. *Adv. Mater.* **2019**, *32*, 1902654. [CrossRef] [PubMed]
14. Naguib, M.; Mochalin, V.N.; Barsoum, M.W.; Gogotsi, Y. 25th anniversary article: MXenes: A new family of two-dimensional materials. *Adv. Mater.* **2014**, *26*, 992–1005. [CrossRef]
15. Handoko, A.D.; Steinmann, S.N.; Seh, Z.W. Theory-guided materials design: Two-dimensional MXenes in electro-and photocatalysis. *Nanoscale Horiz.* **2019**, *4*, 809–827. [CrossRef]
16. Guo, Z.; Miao, N.; Zhou, J.; Sa, B.; Sun, Z. Strain-mediated type-I/type-II transition in MXene/Blue phosphorene van der Waals heterostructures for flexible optical/electronic devices. *J. Mater. Chem. C* **2017**, *5*, 978–984. [CrossRef]
17. Guo, Z.; Zhou, J.; Zhu, L.; Sun, Z. MXene: A promising photocatalyst for water splitting. *J. Mater. Chem. A* **2016**, *4*, 11446–11452. [CrossRef]
18. Fu, C.-F.; Li, X.; Luo, Q.; Yang, J. Two-dimensional multilayer M_2CO_2 (M=Sc, Zr, Hf) as photocatalysts for hydrogen production from water splitting: A first principles study. *J. Mater. Chem. A* **2017**, *5*, 24972–24980. [CrossRef]
19. Zhang, H.; Yang, G.; Zuo, X.; Tang, H.; Yang, Q.; Li, G. Computational studies on the structural, electronic and optical properties of graphene-like MXenes (M_2CT_2, M = Ti, Zr, Hf; T = O, F, OH) and their potential applications as visible-light driven photocatalysts. *J. Mater. Chem. A* **2016**, *4*, 12913–12920. [CrossRef]
20. Shahzad, F.; Alhabeb, M.; Hatter, C.B.; Anasori, B.; Hong, S.M.; Koo, C.M.; Gogotsi, Y. Electromagnetic interference shielding with 2D transition metal carbides (MXenes). *Science* **2016**, *353*, 1137–1140. [CrossRef] [PubMed]
21. Lukatskaya, M.R.; Mashtalir, O.; Ren, C.E.; Dall'Agnese, Y.; Rozier, P.; Taberna, P.L.; Naguib, M.; Simon, P.; Barsoum, M.W.; Gogotsi, Y. Cation intercalation and high volumetric capacitance of two-dimensional titanium carbide. *Science* **2013**, *341*, 1502–1505. [CrossRef] [PubMed]
22. Wang, Y.; Yu, X.; Xu, S.; Bai, J.; Xiao, R.; Hu, Y.-S.; Li, H.; Yang, X.-Q.; Chen, L.; Huang, X. A zero-strain layered metal oxide as the negative electrode for long-life sodium-ion batteries. *Nat. Commun.* **2013**, *4*, 2365. [CrossRef] [PubMed]
23. Peng, Q.; Guo, J.; Zhang, Q.; Xiang, J.; Liu, B.; Zhou, A.; Liu, R.; Tian, Y. Unique lead adsorption behavior of activated hydroxyl group in two-dimensional titanium carbide. *J. Am. Chem. Soc.* **2014**, *136*, 4113–4116. [CrossRef] [PubMed]
24. Khazaei, M.; Arai, M.; Sasaki, T.; Chung, C.Y.; Venkataramanan, N.S.; Estili, M.; Sakka, Y.; Kawazoe, Y. Novel electronic and magnetic properties of two-dimensional transition metal carbides and nitrides. *Adv. Funct. Mater.* **2013**, *23*, 2185–2192. [CrossRef]
25. Zhang, Y.; Xiong, R.; Sa, B.; Zhou, J.; Sun, Z. MXenes: Promising donor and acceptor materials for high-efficiency heterostructure solar cells. *Sustain. Energy Fuels* **2021**, *5*, 135–143. [CrossRef]
26. Hwu, S.J.; Ziebarth, R.P.; Von Winbush, S.; Ford, J.E.; Corbett, J.D. Synthesis and structure of double-metal-layered scandium, yttrium, and zirconium chloride carbides and nitrides, M_2Cl_2C and M_2Cl_2N. *Inorg. Chem.* **1986**, *25*, 283–287. [CrossRef]
27. Zhou, L.; Zhang, Y.; Zhuo, Z.; Neukirch, A.J.; Tretiak, S. Interlayer-decoupled Sc-based MXene with high carrier mobility and strong light-harvesting ability. *J. Phys. Chem. Lett.* **2018**, *9*, 6915–6920. [CrossRef]
28. Maeda, K.; Wakayama, H.; Washio, Y.; Ishikawa, A.; Okazaki, M.; Nakata, H.; Matsuishi, S. Visible-light-induced photocatalytic activity of stacked MXene sheets of Y_2CF_2. *J. Phys. Chem. C* **2020**, *124*, 14640–14645. [CrossRef]
29. Druffel, D.L.; Lanetti, M.G.; Sundberg, J.D.; Pawlik, J.T.; Stark, M.S.; Donley, C.L.; McRae, L.M.; Scott, K.M.; Warren, S.C. Synthesis and electronic structure of a 3D crystalline stack of MXene-like sheets. *Chem. Mater.* **2019**, *31*, 9788–9796. [CrossRef]
30. Blöchl, P.E. Projector augmented-wave method. *Phys. Rev. B* **1994**, *50*, 17953. [CrossRef]
31. Perdew, J.P.; Burke, K.; Ernzerhof, M. Generalized gradient approximation made simple. *Phys. Rev. Lett.* **1996**, *77*, 3865. [CrossRef]
32. Kresse, G.; Furthmüller, J. Efficient iterative schemes for ab initio total-energy calculations using a plane-wave basis set. *Phys. Rev. B* **1996**, *54*, 11169. [CrossRef]
33. Kresse, G.; Joubert, D. From ultrasoft pseudopotentials to the projector augmented-wave method. *Phys. Rev. B* **1999**, *59*, 1758. [CrossRef]
34. Togo, A.; Oba, F.; Tanaka, I. First-principles calculations of the ferroelastic transition between rutile-type and $CaCl_2$-type SiO_2 at high pressures. *Phys. Rev. B* **2008**, *78*, 134106. [CrossRef]
35. Gonze, X.; Lee, C. Dynamical matrices, Born effective charges, dielectric permittivity tensors, and interatomic force constants from density-functional perturbation theory. *Phys. Rev. B* **1997**, *55*, 10355. [CrossRef]
36. Grimme, S.; Antony, J.; Ehrlich, S.; Krieg, H. A consistent and accurate ab initio parametrization of density functional dispersion correction (DFT-D) for the 94 elements H-Pu. *J. Chem. Phys.* **2010**, *132*, 154104. [CrossRef]
37. Wang, G.; Peng, L.; Li, K.; Zhu, L.; Zhou, J.; Miao, N.; Sun, Z. ALKEMIE: An intelligent computational platform for accelerating materials discovery and design. *Comput. Mater. Sci.* **2021**, *186*, 110064. [CrossRef]
38. Furche, F.; Ahlrichs, R. Adiabatic time-dependent density functional methods for excited state properties. *J. Chem. Phys.* **2002**, *117*, 7433–7447. [CrossRef]
39. Marsman, M.; Paier, J.; Stroppa, A.; Kresse, G. Hybrid functionals applied to extended systems. *J. Phys. Condens. Matter* **2008**, *20*, 064201. [CrossRef]
40. Zacharia, R.; Ulbricht, H.; Hertel, T. Interlayer cohesive energy of graphite from thermal desorption of polyaromatic hydrocarbons. *Phys. Rev. B* **2004**, *69*, 155406. [CrossRef]
41. Miao, N.; Xu, B.; Zhu, L.; Zhou, J.; Sun, Z. 2D intrinsic ferromagnets from van der Waals antiferromagnets. *J. Am. Chem. Soc.* **2018**, *140*, 2417–2420. [CrossRef] [PubMed]

42. Sun, Z.; Music, D.; Ahuja, R.; Li, S.; Schneider, J.M. Bonding and classification of nanolayered ternary carbides. *Phys. Rev. B* **2004**, *70*, 092102. [CrossRef]
43. Chakrapani, V.; Angus, J.C.; Anderson, A.B.; Wolter, S.D.; Stoner, B.R.; Sumanasekera, G.U. Charge transfer equilibria between diamond and an aqueous oxygen electrochemical redox couple. *Science* **2007**, *318*, 1424–1430. [CrossRef] [PubMed]
44. Green, M.A.; Keevers, M.J. Optical properties of intrinsic silicon at 300 K. *Prog. Photovolt. Res. Appl.* **1995**, *3*, 189–192. [CrossRef]
45. American Society for Testing and Materials; Committee G03 on Weathering and Durability. *Standard Tables for Reference Solar Spectral Irradiances: Direct Normal and Hemispherical on 37° Tilted Surface*; ASTM International: West Conshohocken, PA, USA, 2012. [CrossRef]
46. Zhang, H.; Wu, D.; Tang, Q.; Liu, L.; Zhou, Z. ZnO–GaN heterostructured nanosheets for solar energy harvesting: Computational studies based on hybrid density functional theory. *J. Mater. Chem. A* **2013**, *1*, 2231–2237. [CrossRef]